**Research Article**

# Experimental and numerical study of fluid flow and heat transfer in the impinging of inline round jets

## B. Venkata Sai Raghu VAMSI[1],*⬛, P. RAVEENDIRAN[1]⬛, Malladi R. Ch. SASTRY[2]⬛

*[1]Department of Mechanical Engineering, Annamalai University, Tamil Nadu, 608002, India*
*[2]Department of Mechanical Engineering, Seshadri Rao Gudlavalleru Engineering College, Andhra Pradesh, 521356, India*

**ABSTRACT**

The effect of pitch-to-diameter ratio, dimensionless nozzle-to-plate spacing, and Reynold's number on fluid flow behavior and heat transfer from the heated surface is studied numerically for three inline circular impinging jets. The dimensionless nozzle to distance varies from 1 to 6, the pitch-to-diameter ratio from 2 to 4, and Reynold's number from 3512.69 to 9532.71. The streak lines plotted numerically are validated by experiments using the Oil flow visualization technique. As the inter-jet spacing increases, a shift in the direction of the resultant fluid flow on the target surface is observed with a symmetrical distribution of fluid flow and heat transfer at P/D=4.Correlations for the maximum static pressure, maximum coefficient of pressure, and average Nusselt number on the target surface are proposed by performing regression analysis at a confidence level of 98% with an $R^2$ value of 99.53%, 99.60%, and 99.21%, respectively. In addition, it has been observed that the jet-to-jet distance, distance between the nozzle and target plate, and Reynold's number play a crucial role in the augmentation of heat transfer and distribution of air in the multiple impinging jets.

**Cite this article as:** Vamsi BVSR, Raveendiran P, Sastry MRC. Experimental and numerical study of fluid flow and heat transfer in the impinging of inline round jets. J Ther Eng 2025;11(1):270–289.

## INTRODUCTION

Jet impingement is a fluid dynamics phenomenon wherein a high-velocity fluid jet strikes a solid surface. This interaction generates intense forces and heat transfer due to rapid momentum exchange. Jet impingement enhances heat dissipation and mixing commonly utilized in applications such as cooling systems and industrial processes. The impinging jet's impact zone influences heat transfer efficiency and fluid dynamics, making it a critical element in various fields, including aerospace, manufacturing, and electronics cooling. Understanding and optimizing jet impingement is essential for designing efficient thermal management and energy transfer systems. Garimellaet al. [1] conducted experiments to study the behavior of the shower of impinging round jets onto a flat surface and proposed correlations to calculate the average Nusselt number. Aldabbagh and Sezai [2] investigated the influence of dimensionless nozzle-to-plate spacing and inter-jet spacing

*Corresponding author.
*E-mail address: drbvsraghuvamsi@gmail.com

on the flow behavior and transfer of heat in the imping-ing of multiple square jets numerically. The impact of the nozzle geometry configuration on the hydrodynamic and thermal behavior of the array of submerged jets imping-ing on a surface over Reynold's number range of 1000-7700 was examined by Royne and Dey [3]. Rama Kumar et al. [4, 5] compared the characteristics of fluid flow and transfer of heat in the impingement of single and multiple arrays of circular jets on a concave surface, experimentally and numerically. Raoet al. [6, 7] investigated the impinge-ment of jets in numerous rows with various configurations experimentally and numerically. They found that SST k-ω is the suitable turbulent model for multiple impinging jets. Afroz and Sharif [8] presented the analysis of inclined twin jets onto a flat surface numerically at higher Reynolds num-bers of 23000 and 50000. They observed that the turbulence model SST k-ω predicts the heat transfer nearer to exper-imental results. In addition, it has been observed that the average Nusselt number strongly depends on the Reynolds number and angle of impingement. Hossain et al. [9] ana-lyzed the performance of a row of impinging jets in a nar-row channel at Reynold's number of 30000 experimentally. The influence of dual jets impinging on a hot surface was numerically studied by Nabadavis and Mishra [10]. They discovered that a greater heat transfer rate can be achieved when the jets are slanted as opposed to orthogonal. Meena et al. [11] examined the dependence of transfer of heat on the shape of the orifice and found that circular jets provide heat transfer higher than triangular and square jets.

Shariatmadaret al. [12] subjected a series of imping-ing jets to numerical and experimental examination. They discovered that the large nozzle-to-plate separation and lesser flow rate are the causes of the impingement plate's uneven cooling. Attalla et al. [13] studied the performance of the inline impinging jets and reported that the circular jets delivered higher heat transfer than square jets for the same hydraulic diameter. Simionescuet al. [14] studied the dynamic characteristics of the impinging air jets on flat surfaces numerically and experimentally. Kannan and Panchapakesan [15] reported that the widening of the mix-ing region and secondary flows is due to the higher momen-tum flux produced around the multiple jets under turbulent flow conditions. Culunet al. [16] presented a comparative analysis of numerous impinging jets. They discovered that when one side of the exit is constrained, the pattern of flow resembles that of an impinging single jet, and a square jet outperforms a circular jet. Barbosa et al. [17] evaluated the performance of the numerous impinging jets by varying the inter-jet spacing, plate-to-nozzle spacing, Reynold's num-ber, and target plate conditions by applying the Taguchi method. Shah [18] reported the analysis of inline imping-ing jets on an even surface in motion at Reynold's num-ber of 26000 numerically. Lahaneet al. [19] experimentally examined the impingement of a mixture of ethylene glycol with water onto a heated surface.

Ingole [20] reported that the inclination angle signifi-cantly affects the transfer of heat in jet impingement. Kilic and Ali [21] conducted a numerical analysis to study the effect of volume ratio, heat flux, and type of nanofluid on the augmentation of heat transfer and flow behavior in the impingement of 3-jets onto a heated surface. Kilic and Abdulvahitoglu [22] studied the performance of imping-ing swirling jets and nano-fluids in a radiator, numerically. Kilic and Baskaya [23] analyzed that the inclusion of turbu-lence promoters (shapes viz., cylinder, square, and triangle) enhanced the transfer of heat from the hot surface by 28% when combined with the impinging jets. Kilic and Ozcan [24] reported that the enhancement of heat transfer is sig-nificantly affected by the size of the nano-particle size and Reynold's number. The conjugate heat transfer phenome-non on the impingement of air jets over a nozzle guide vane was quantitatively documented by Kukutla and Prasad [25]. Furthermore, a theoretical and experimental study of the joint performance of film cooling and secondary air-flow via a staggered array of impinging jets is conducted [26]. Additionally, they have published a 1-D study on the impact of a jet network on the cooling of a high-pressure gas turbine's first-stage guide vane [27].

To understand the behavior of fluid stream and transfer of heat in the impingement of numerous jets, it is possible to examine jet interactions and flow patterns at different Reynolds numbers, dimensionless inter-jet distance, and plate-to-nozzle spacing. The flow visualization test gives an insight into the interaction between the jets by observing the flow patterns on the target plate. This clearly explains the heat transfer mechanism from the target surface to the air, which is not discussed thoroughly in the literature. Hence, the broad objectives of this study are therefore to (i) study the flow structure of the impinging jets, (ii) study the influence of varying H/D, P/D, and Re on the Pressure and Nu, (iii) compare the transfer of heat and pressure drop in single and multiple jets. The experimental setup utilized to depict the flow structures is described in Section 2, and Section 3 presents the particulars of the numerical analysis, including data reduction and grid-independent examina-tion. The explanation of the findings and the created cor-relations is included in Section 4.

## EXPERIMENTAL SETUP

Figures 1(a) and 1(b) depict the experimental setup employed in this study. Initial compressed air, generated by a two-stage reciprocating air compressor, is released upon opening the flow control valve. The ensuing airflow is quan-tified using a rotameter. Subsequently, the compressed air is directed through a diverging segment, converting pressure to kinetic energy. This high-velocity air is then directed onto the test area via an impingement chamber with three orifice holes shown in Figure 2(a), meticulously fabricated through laser jet machining on a stainless-steel plate. The test area comprises an adjustable flat stainless-steel plate

above a height-regulating system incorporating a lead screw mechanism, allowing for precise adjustments as small as 0.5 mm. Figure 1(c) illustrates the mechanism of energy transmission in the test plate. Joulean heating is performed with an electrical plate-type heater located below the target plate. When the current is flowing through the heater, it is dissipated as heat by conduction through the target plate and insulation, by radiation and convection from the top of the target surface. Except for the top surface of the stainless-steel plate, all sides are insulated with Aluminum Silicate, which has a thermal conductivity of 0.03 W/m-K. The input to the heater plate is adjusted by using a dimmerstat. The surface temperature of the test section is measured

by inserting K-type thermocouples into the plate from the bottom surface. Uncertainty analysis is used to estimate the error in temperature measurement. The range of values considered for variables is presented in Table 1.

The thermocouples were calibrated by immersing them into a hot water bath, alongside a mercury thermometer. The average error in the temperature measurement was 0.67%. The temperature of the jet was measured at the nozzle outlet, and the error in the jet temperature was 1.33%. The uncertainty in surface temperature measurement was found to be 1.3%, and the radiation losses were 0.5% of the input. Air impinged onto the plate at a mass flow rate of 0.00119 kg/s for the H/D = 2, and the average
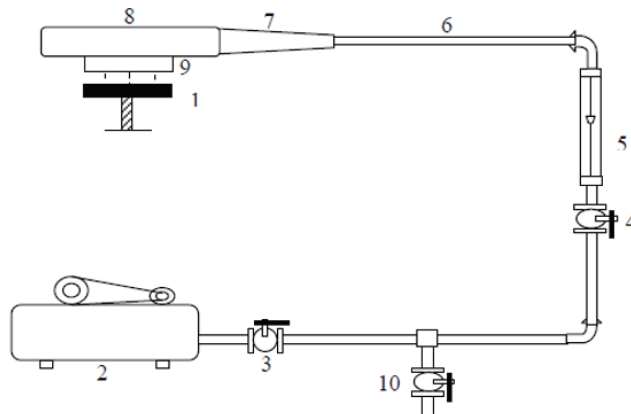


1. Test section 2. Compressor 3. Ball valve 4. Needle valve 5. Rotameter 6. Hose pipe 7. Diverging section
8. Plenum chamber 9. Impingement chamber 10. Bypass line.

**Figure 1. (a)** Schematic diagram of overall experimental setup.
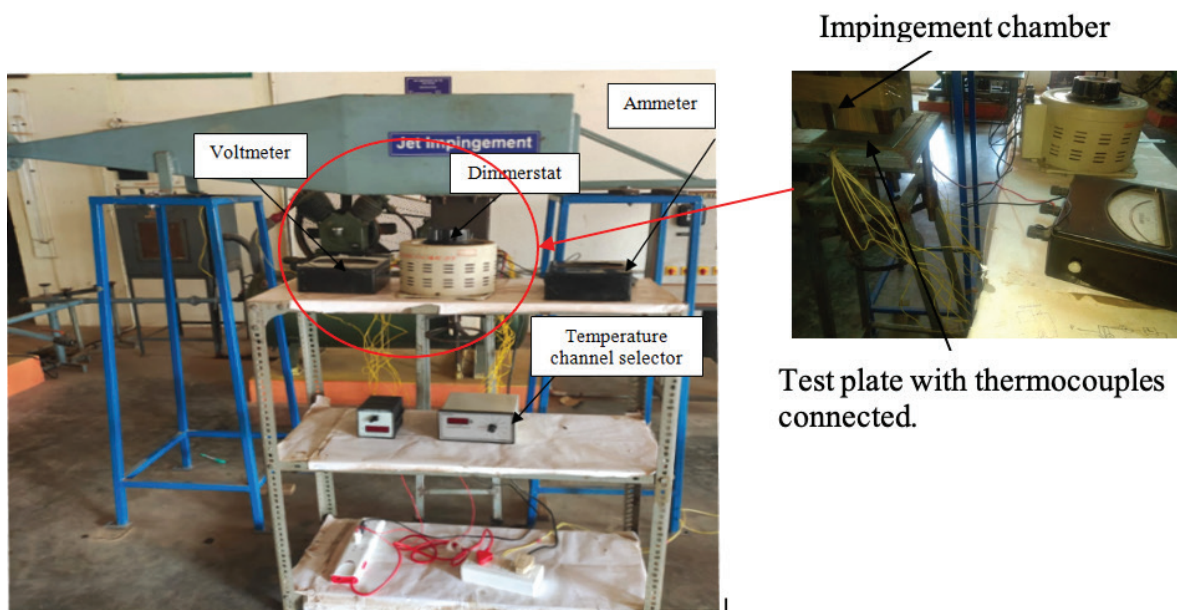


**Figure 1. (b)** Actual experimental setup.
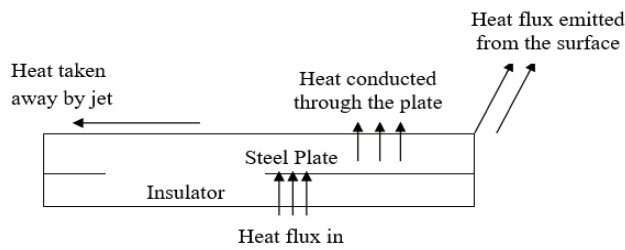
**Figure 1. (c)** Mechanism of energy transfer.

**Table 1.** Parameters varied

| S.No | Parameter | Range of values |
|------|-----------|-----------------|
| 1 | Aspect ratio | 1 (Geometry is a circle) |
| 2 | H/D | 1, 2, 4, 6 |
| 3 | D at the inlet (m) | 0.008 |
| 4 | P/D | 2, 3, 4 |
| 5 | Re | 3512.69, 5017.69, 6522.7, 8027.71, 9532.71 |

rise in the surface temperature at the point of impingement was 2.33°C. The $Nu_{stag}$ was calculated three times, and the uncertainty was 2.19%. As the H/D increased, the temperature rise decreased. The peak Nu shifted towards the stagnation point due to the expansion of the jet along the spanwise direction on the target plate and the loss of jet velocity to the surroundings.

## Numerical Analysis and Methodology

The following section describes the adopted boundary constraints and the grid-independent analysis. Figure 2(a) illustrates a computational model with dimensions and heat flux arbitrarily selected for depiction. The hydraulic diameter (D) remains consistent at 8 mm upon entry. Inflation is applied at the confinement wall and target surface wall to capture the gradients near the wall so that the mesh is sufficiently refined, and care is taken to ensure the y+ value is in the range of 0.1 – 0.18 across all simulations. The meshed view of the computational domain is presented in Figure 2(b). The stable, pressure-based solver is employed. The SST k-ω turbulent model has been implemented to solve the conservation equations for establishing the flow and temperature fields of the impinging jets based on the literature that is currently accessible. The SIMPLE scheme is employed to define the relationship between velocity and pressure. The second-order upwind approach is used to solve the energy and momentum equations. In contrast, the first-order upwind scheme solves the specific dissipation rate (ω) and turbulent kinetic energy (k). To obtain the convergence, all residuals for the momentum, continuity, ω, and k-ω equations are adjusted to $10^{-6}$ whereas $10^{-8}$ is set for the energy equation. The final solution is considered when these residual criteria are satisfied. Further, the area weighted average of the pressure on the impingement surface is continuously monitored, so that the variation will be within 0.1% for 1000 consecutive iterations. A total of sixty simulations are executed, encompassing the permutations
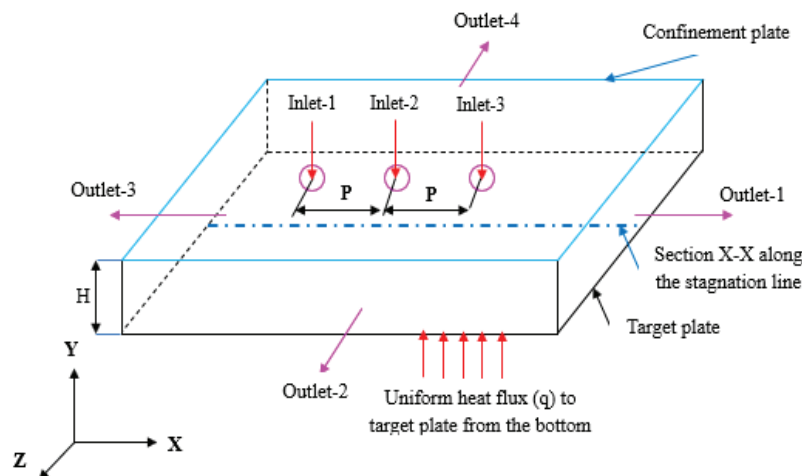


**Figure 2. (a)** Computational model of the problem.
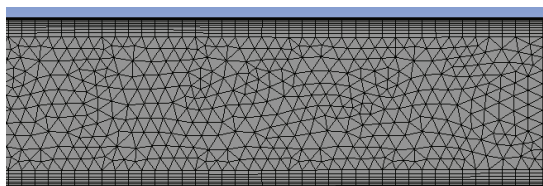


**Figure 2. (b)** A meshed view of the model.

detailed in Table 1and the boundary conditions considered are presented in Table 2.

Two-dimensional turbulent incompressible steady flow is assumed. The flow pattern and heat transfer distribution over the heated flat surface are predicted using the Reynolds time Averaged Navier-Stokes (RANS) equations. The continuity, momentum, and energy equations are used for numerical simulation with minimal external force.

$$\frac{\partial u_i}{\partial x_i} = 0.  \tag{1}$$

$$\rho u_j \frac{\partial u_i}{\partial x_j} = -\frac{\partial P}{\partial x_i} + \frac{\partial}{\partial x_j}\left[\mu\left(\frac{\partial u_i}{\partial x_j} + \frac{\partial u_j}{\partial x_i}\right) - \rho\overline{u_i'u_j'}\right].  \tag{2}$$

$$\rho u_j \frac{\partial T}{\partial x_j} = \frac{\partial}{\partial x_j}\left[\frac{\mu}{\Pr}\frac{\partial T}{\partial x_j} - \rho\overline{u_j'T'}\right].  \tag{3}$$

The turbulent shear stress and the heat flux can be calculated from Boussinesq's hypothesis using the following relations,

$$-\rho\overline{u_i'u_j'} = \mu T\frac{\partial u_i}{\partial x_j}  \tag{4}$$

$$-\rho\overline{T'u_j'} = \frac{\mu_T}{\Pr_T}\frac{\partial T}{\partial x_j}  \tag{5}$$

The turbulence Prandtl number $\Pr_T$ is taken as constant for the numerical analysis.

The typical k-ω model, created by Wilcox [29], is extremely sensitive to inlet free stream turbulence. Using a blending function F1, Menter and Esch [30] converted the standard k-ε model into the k-ω form. As a result, the model uses the blending function $F_1$ to combine the benefits of the k-ε and k-ω models. Close to the walls, the value of $F_1$ is one and zero for the remaining portion of the flow [31]. The transport equations of the SST k-ω turbulence model are

$$\rho u_i \frac{\partial k}{\partial x_i} = \tilde{P}_k - \beta*\rho k\omega + \frac{\partial}{\partial x_i}\left[\left(\mu + \sigma_k\mu_T\right)\frac{\partial k}{\partial x_i}\right]  \tag{6a}$$

$$\rho u_i \frac{\partial \omega}{\partial x_i} = \alpha\rho S^2 - \beta\rho\omega^2 + \frac{\partial}{\partial x_i}\left[\left(\mu + \sigma_\omega\mu_T\right)\frac{\partial \omega}{\partial x_i}\right]$$
$$+ 2\left(1 - F_1\right)\rho\sigma\omega_2\frac{1}{\omega}\frac{\partial k}{\partial x_i}\frac{\partial \omega}{\partial x_i}  \tag{6b}$$

The blending function $F_1$ is defined as:

$$F_1 = \tanh\left[\left[\min\left(\max\left(\frac{\sqrt{k}}{\beta*\omega y}, \frac{500\upsilon}{y^2\omega}\right), \frac{4\rho\sigma_{\omega 2}k}{CD_{k\omega}y^2}\right)\right]^4\right]  \tag{6c}$$

$$CD_{k\omega} = \max\left(2\rho\sigma_{w2}\frac{1}{\omega}\frac{\partial k}{\partial x_i}\frac{\partial \omega}{\partial x_i}, 10^{-10}\right)  \tag{6d}$$

The turbulent viscosity can be calculated as

$$\upsilon_\tau = \frac{\alpha_1 k}{\max\left(\alpha_1\omega, SF_2\right)}  \tag{6e}$$

Blending function $F_2$ is defined as

$$F_2 = \tanh\left[\left[\max\left(\frac{2\sqrt{k}}{\beta*\omega y}, \frac{500\upsilon}{y^2\omega}\right)\right]^2\right]  \tag{6f}$$

The production limiter, defined as follows, prevents the development of turbulence in the stagnation region.

$$P_k = \mu_\tau\frac{\partial u_i}{\partial x_j}\left(\frac{\partial u_i}{\partial x_j} + \frac{\partial u_j}{\partial x_i}\right)  \tag{6g}$$

$$\tilde{P}_k = \min\left(P_k, 10\beta*\rho k\omega\right)  \tag{6h}$$

The model constants' values are.

| $\beta*$ | $\sigma_{k1}$ | $\sigma_{\omega 1}$ | $\alpha_1$ | $\beta_1$ | $\sigma_{k2}$ | $\sigma_{\omega 2}$ | $\alpha_2$ | $\beta_2$ |
|---|---|---|---|---|---|---|---|---|
| 0.09 | 0.85 | 0.5 | 0.59 | 0.075 | 1 | 0.856 | 0.44 | 0.0828 |

**Table 2.** Boundary conditions

| Boundary | Condition |
|---|---|
| Inlet | Mass flow rate (kg/s), Turbulence Intensity (%), Hydraulic Diameter (D) |
| Outlet | Gauge Pressure (Pa), Turbulence Intensity (%), Hydraulic Diameter (D) |
| Bottom wall | No-slip condition, Heat flux input |
| Top Wall | No-slip condition, Adiabatic condition |

**Data Reduction**

A dimmerstat controls the energy input to the heater, and an ammeter and voltmeter measure the supplied current (I) and voltage (V). The heat flux supplied is calculated as

$$q = \frac{V \times I}{A} \, W/_{m^2}. \tag{7}$$

Reynold's number is calculated using a single nozzle with a mass flow rate of m as

$$Re = \frac{4m}{\pi D \mu}. \tag{8}$$

After the simulation, a section line X-X is taken on the target surface along the x-axis at the center of the plate, as shown in Figure 2(a). The target surface's temperature (Ts) is measured along this section line, and the relation estimating the heat transfer coefficient at various points along the section x-x is.

$$h_x = \frac{q}{(T_s - T_a)}. \tag{9}$$

The corresponding Nusselt number is computed using.

$$Nu = \frac{h_x D}{k_{air}}. \tag{10}$$

The computation of the typical heat transfer coefficient is

$$h_{avg} = \frac{1}{L} \int_0^L h_x dx. \tag{11}$$

The average Nusselt number is calculated as

$$Nu_{avg} = \frac{h_{avg} D}{k_{air}}. \tag{12}$$

The pressure coefficient (Cp) is characterized as the ratio of static pressure to dynamic pressure at the nozzle inlet. In this work, the pressure coefficient is calculated at the stagnation point and hence it is maximum.

$$(Cp)_{max} = \frac{2P_{max}}{\rho V^2} \tag{13}$$

**Grid Independent Study**

The fluid domain was meshed with tetrahedron elements. Through the execution of a grid-independent investigation, the effect of element size on the solution's precision will be investigated. It is carried out for H/D = 2, Re = 3512.69, and P/D = 4. The study uses the SST k-ω turbulent model for various element sizes, and Table 3 shows the percentage change in the mean heat transfer coefficient value. The mean heat transfer coefficient significantly changed when the element count climbed from 0.93 to 2.51 million. The mean heat transfer coefficient changed by a relatively small percentage when the elements increased by more than 2.51 million. Therefore, in further study, an element size of 0.0014 m, equivalent to 2.51 million, is employed to reduce the computation time, giving an advantage.

Figure 2(c) compares SST k-ω results to RNG k-ε and Realizable k-ε turbulence models, as well as experimental values, for this grid size. The comparison is done for H/D=6, P/D=4 and Re=9532.71. The turbulence models RNG k-ε and Realizable k-ε underestimated the Nu along section line X-X. The SST k-ω model produced results that were consistent with experimental data. The SST k-ω overpredicted the Nu by less than 2% in the stagnation region. To conduct additional research, the SST k-ω turbulence model is used.
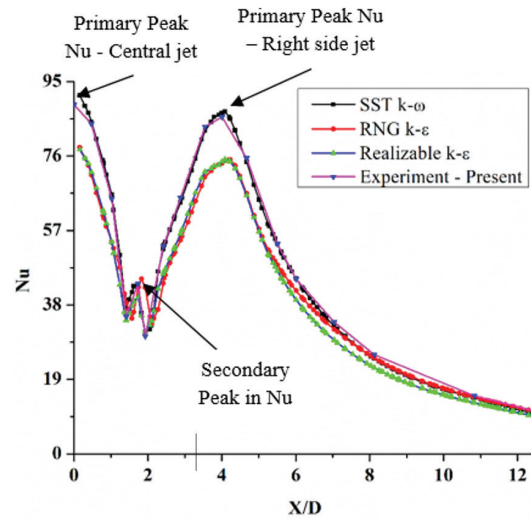


**Figure 2.** (c) Comparison of turbulence models and validation.

**Table 3.** Grid independent study

| S.No | No. of Elements (x 10⁶) | Ts (avg) (°C) | $h_{avg}$ (W/m²-K) | % change |
|------|--------------------------|---------------|---------------------|----------|
| 1 | 0.93 | 335.7879 | 55.87 | -- |
| 2 | 1.71 | 334.4376 | 58.08 | -3.96 |
| 3 | 2.51 | 337.0192 | 54.03 | 6.97 |
| 4 | 3.21 | 337.0159 | 54.04 | -0.02 |

## RESULTS AND DISCUSSION

This section discusses the velocity, pressure, and Nu distribution over the target plate at H/D=1 to 6, P/D=2 to 4, and Re=3512.69 to 9532.71.

### Velocity Distribution

Figures 3(a) to 3(f) represent the distribution of velocity at Re=3512.69 for H/D=1&6 and P/D=2 to 4, whereas Figures (g) to (j) at H/D=6, P/D=4 for Re=5017.9 to 9532.71 in the vertical plane passing through the section X-X taken along the stagnation points. At H/D=1, it can be understood from Figures 3(a) to 3(c) that the jet leaving the nozzle strikes the target plate and distributes in the lateral direction along the surface. The jets interact with the adjacent jets, mixing and resulting in upwash flow in the region of the wall jet. As a result of this mixing, turbulence becomes more intense, accelerating the heat transmission rate. Then, the upwash flow strikes the confinement plate and mixes with the free jet issuing from the nozzles. Hence, the spent jet is continuously mixed with the issuing free jet at the lower nozzle-to-plate distances. Figure 3(a) shows that two vortices are formed between the outer and the central jets, of smaller sizes at P/D=2, one having clockwise rotation towards the central jet and another with counterclockwise rotation towards the exterior jet.



(a) H/D=1, P/D=2, Re=3512.69

(b) H/D=1, P/D=3, Re=3512.69

(c) H/D=1, P/D=4, Re=3512.69

(d) H/D=6, P/D=2, Re=3512.69

(e) H/D=6, P/D=3, Re=3512.69

(f) H/D=6, P/D=4, Re=3512.693

(g) H/D=6, P/D=4, Re=5017.9

(h) H/D=6, P/D=4, Re=5017.9

(i) H/D=6, P/D=4, Re=8027.71

(j) H/D=6, P/D=4, Re=5017.9
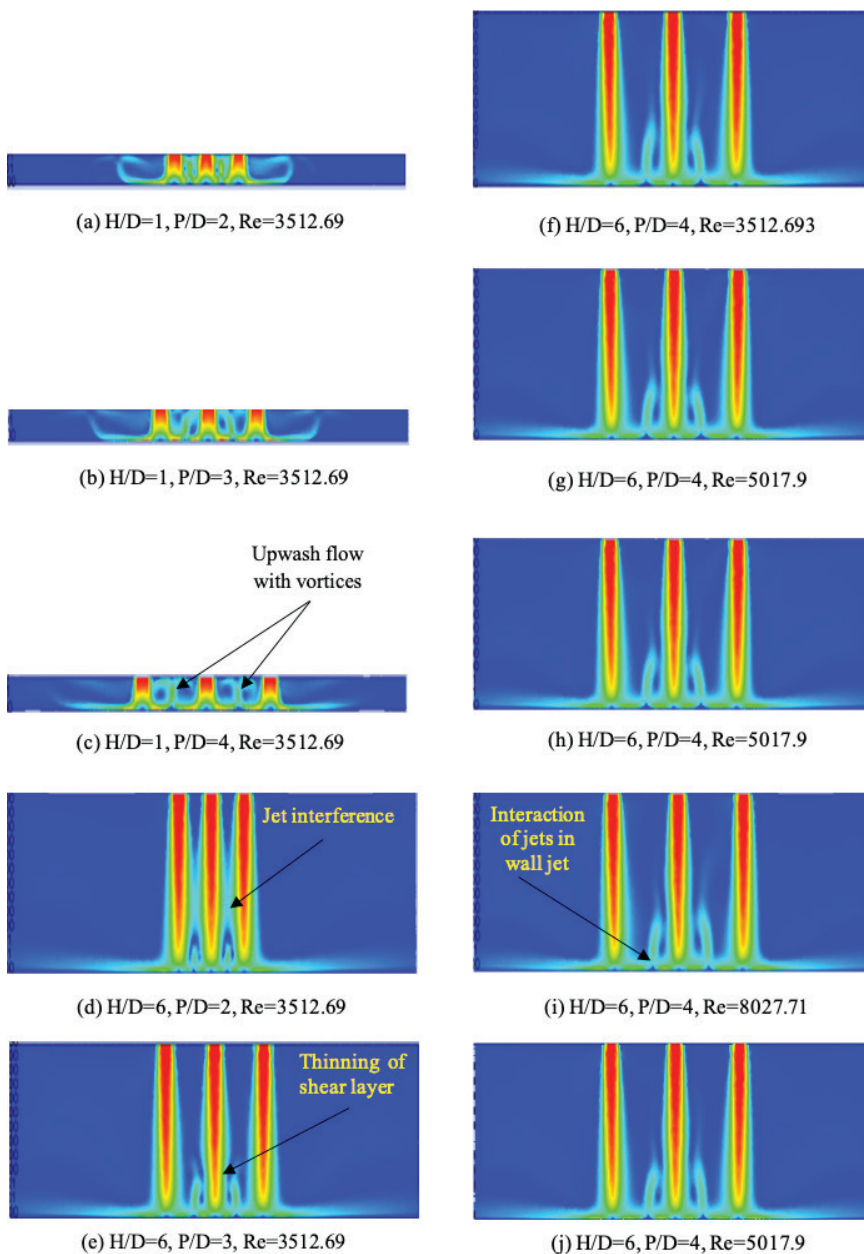
**Figure 3.** Velocity distributions in the vertical plane passing through the section line X-X.

As the inter-jet spacing increases, the size of the vortices increases for a given Re, with maximum occurring at P/D=4 from Figure 3(c). This can be due to the enhanced exchange of momentum with surroundings. Away from the outer jets, large vortices are formed on either side, creating an inward flow towards the outer jets. At P/D=2, these vortices are observed to be strong and become weak at P/D=4.The momentum transmission to the surroundings increases as the H/D rises. For H/D=6, from Figure 3(d), it is evident that the thickness of the shear layer surrounding the potential core increased initially and later diminished for the inner jet due to the interaction between the inner and outer jets. The outer jets expand inwards to the main jet, thus thinning the shear layer. After striking the plate, upwash flow is produced, but the spent air rises to less altitude. The shear layer thickness for the outer jets steadily increased, reaching its maximum near the target surface.

From Figure 3(e) at P/D=3, we can observe that the jet interactions reduced before striking the plate. In the zone of the wall jet, the motion of the spent air in the upward direction is towards the middle jet, forming two counter-rotating vortices on either side of the middle jet. The shear layer surrounding the inner jet is thinned towards the target surface due to the outer jet's crossflow towards the central jet in the wall jet area. A growth in the vortex size is noticed with an increase in the nozzle-to-nozzle distance from P/D=2 to 4, visible in Figures 3(e)-3(f). The effect is more air flowing along the central jet, leading to higher heat transfer at the stagnation point. So, at higher nozzle-to-plate spacing, at the middle jet, the Nu is higher than at the outer jets, as visible in Figures 6(g) and 6(h). This phenomenon is strong at P/D=4 from Figure 3(f) and reported higher Nu at the central jet than P/D=2 and 3. In contrast, the impinging velocity of the central jet decreases, resulting in less static pressure at the point of stagnation compared to the outer jets. This is visible in Figure 4(l). For the H/D=6 and P/D=4, as the Re increased from 3512.59 to 9532.71, the above-discussed effect is observed, with an enhanced elevation in the secondary stream of spent air between the central and outer jets. At higher Re, due to the more
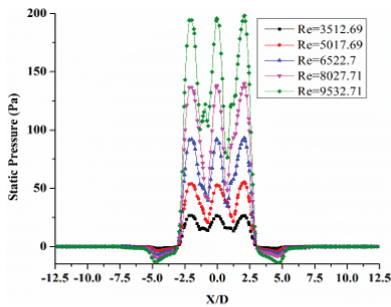


(a) P/D=2, H/D=1
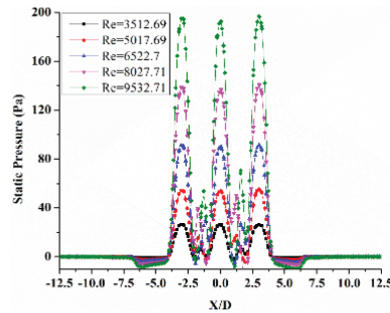
(b) P/D=3, H/D=1
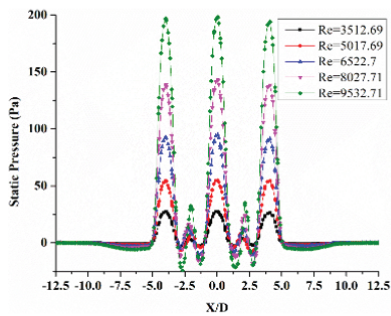
(c) P/D=4, H/D=1
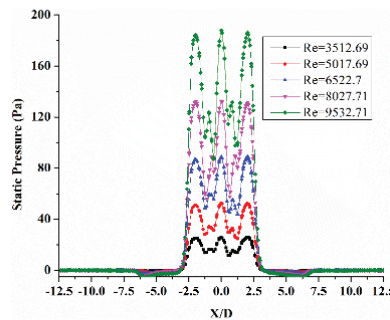
(d) P/D=2, H/D=2

(e) P/D=3, H/D=2

(f) P/D=4, H/D=2

(g) P/D=2, H/D=4

(h) P/D=3, H/D=4

(i) P/D=4, H/D=4

(j) P/D=2, H/D=6

(k) P/D=3, H/D=6

(l) P/D=4, H/D=6
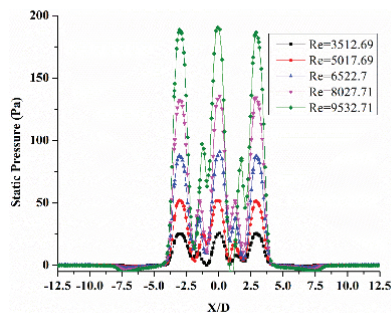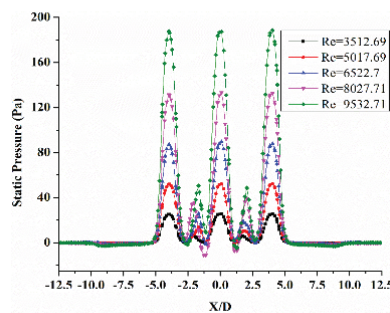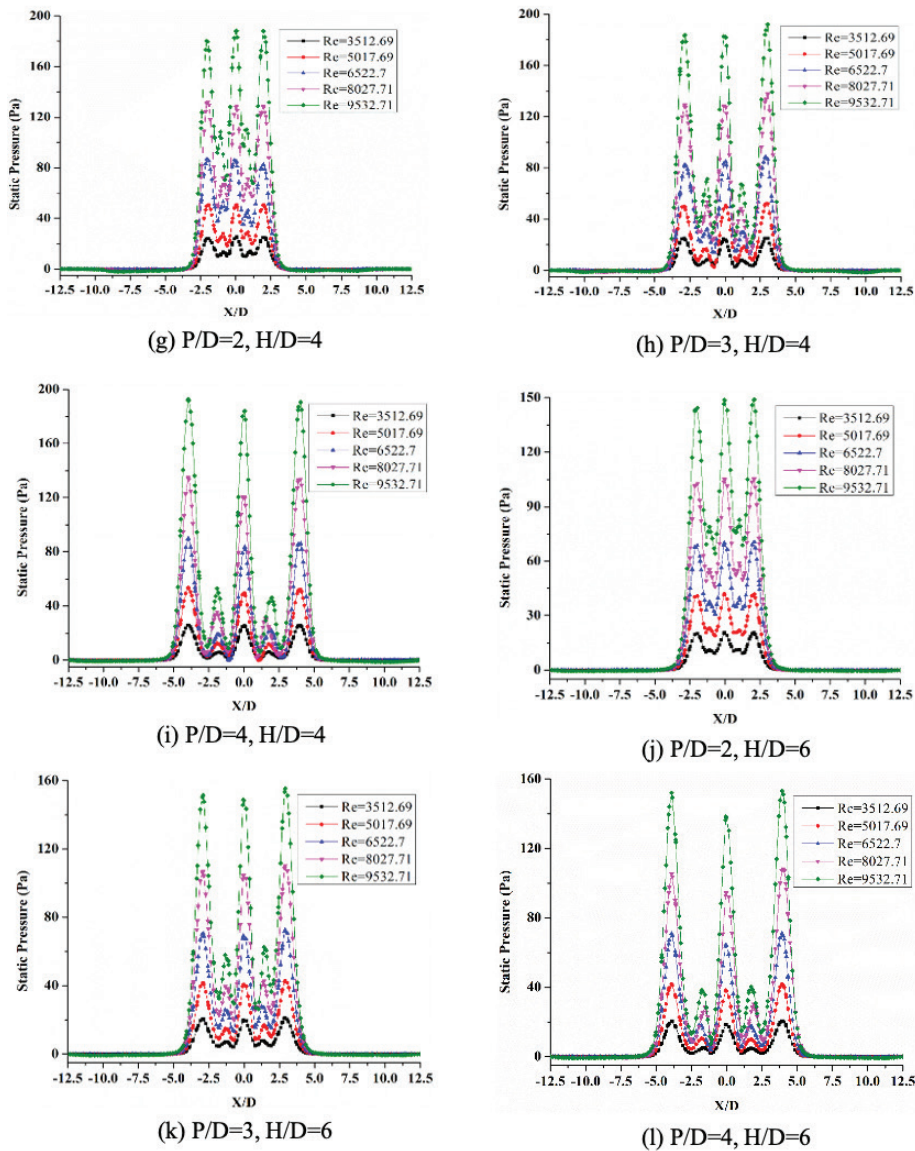
**Figure 4.** Static Pressure distribution along the section x-x on the target plate.

entrainment towards the central jet, a bending of the outer jets towards the inner jet is observed in Figure 3(j). This trend is like Rao et al.'s [6].

**Pressure Distribution**

The span-wise distribution of static pressure along section x-x is presented for all H/D, P/D, and Re in Figures 4(a) – 4(l). At P/D=2, the jet interference is significant before striking the surface. Due to interference, more momentum exchange is observed in the lateral direction from the middle jet to the outer jets. This reduces the pressure at the point of the jet striking the plate, called the stagnation point, producing a primary peak. Hence, the stagnation pressure of the middle jet is not equal to that of the outer jets. This made the pressure distribution unsymmetrical about the center of the plate. This trend of pressure distribution is

also reported by Rama Kumar and Prasad [5], which can be due to the difference in the momentum exchange with surroundings by the central and outer jets. Away from the outer jets, low-pressure zones are created at H/D=1, whose strength decreases gradually as the target plate moves away from the nozzles. Also, after striking the plate, the jets interact, increasing the pressure and giving rise to a secondary peak, creating an upwash flow. With increased separation between the jets (P/D>2), the effect of interference between the jets away from the plate is reduced, and the momentum transfer from the central jet to the outer jets. However, the interference became strong slightly away from the plate due to the span-wise distribution of the jet above the target surface, increasing turbulence. Hence, it resulted in more momentum transfer from the central jet to the surrounding jets, thus reducing the peak stagnation pressure at the
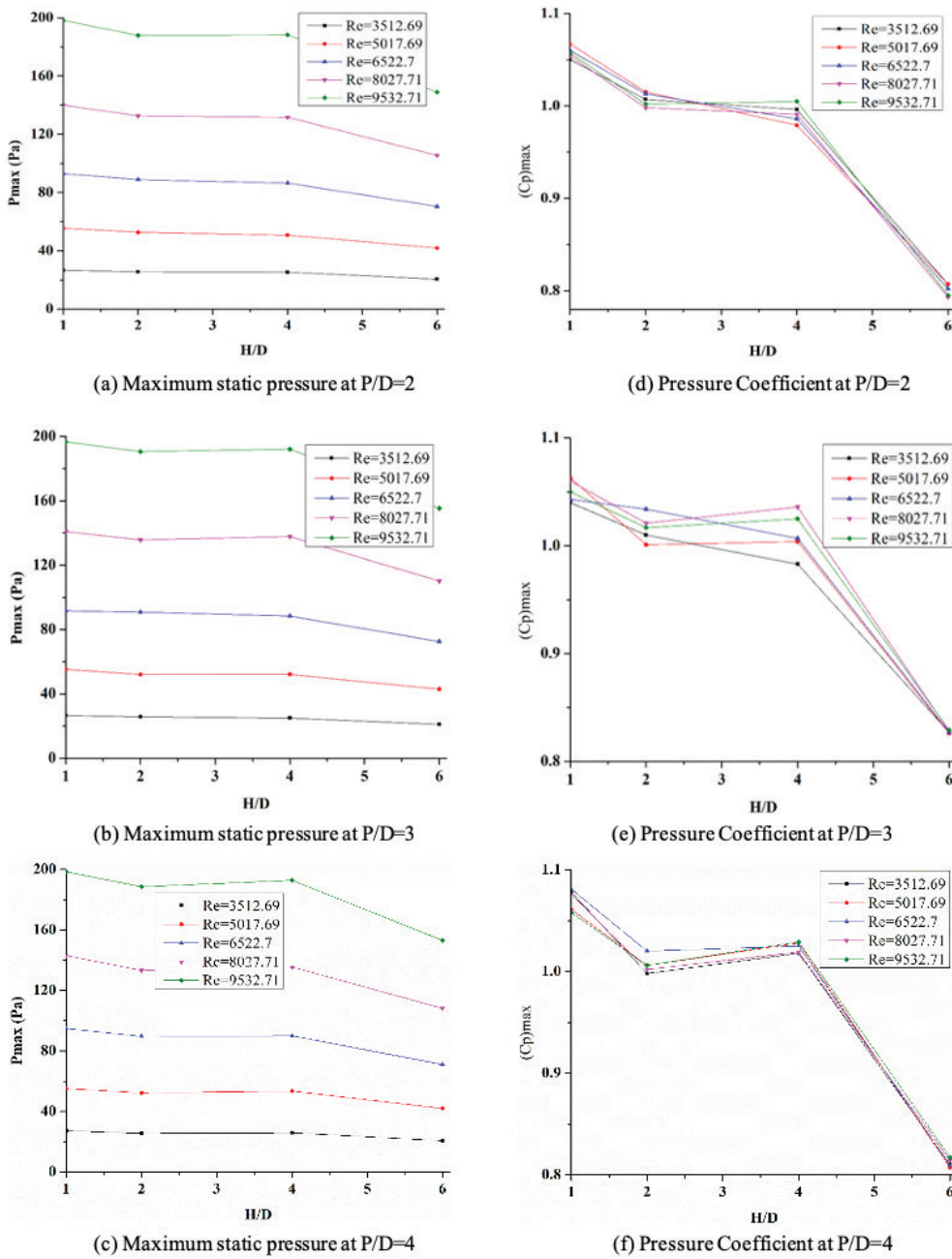
**Figure 5.** Variation of Pmax and (Cp)max.

central jet compared to the outer jets. The asymmetry in the pressure distribution is decreased slightly, but a specific location of the secondary peak is observed. Slight asymmetry in the pressure distribution is observed at P/D=3. In contrast, complete symmetry in the distribution of pressure about the middle jet is noticed at P/D =4 from Figures 4(c), 4(f), 6(i), and 6(l). This phenomenon is the same for H/D= 1 to 6 for all P/D and Re. A surge in the H/D resulted in a decrease in the pressure on the plate. The maximum value of pressure in the primary peak and the secondary peak is

observed at H/D=1, whereas the minimum is observed at H/D=6.

At Re=3512.69, the secondary maximum is located closer to the central stream on both sides, but with an increase in the Re, the location is shifted towards the middle of the adjacent jets. These primary peak and secondary peak pressure values are less at Re=3512.69. An increase in the Re increased the pressure value at the stagnation point. The highest-pressure value of the primary peak is observed at Re=9532.71 at outer jets at P/D=2 and the minimum value at the central jet at P/D=4 from Figure 4(l). In contrast, the

maximum pressure value of the secondary peak is observed at Re=9532.71 between outer and mid jets at P/D=2 and the minimum value at the central jet at P/D=4.

Additionally, from Figure 10(a), when the pressure distribution at Re=9532.71 is compared for P/D=2, 3, 4, and 5, a distinct secondary peak is seen in the range of 1.2<X/D<2.5 for all cases. This secondary peak is caused by the interaction of the jets in the wall jet region, which changes the flow in the boundary layer from laminar to turbulent. The maximum drop in the Cp is noticed when the H/D increased from 4 to 6 for all P/D and Re, visible in Figure 5. In contrast, for a given H/D, with an increase in the Re, the Cp remained constant, i.e., Cp is independent of Re. This trend is also reported by Attalla et al. [13] and other authors. It has been noted that the maximum pressure (Pmax), caused by the high impact velocity, increased with an increase in the Re but dropped with an increase in the H/D, caused by the loss of momentum to the surroundings. Increase in the dimensionless inter-jet separation P/D, the variation in the Pmax is less than 2% for all Re. Hence, P/D has a negligible effect on the Pmax. With an increase in the H/D from H/D=1 to 2, Pmax decreased slightly, and then the change from H/D=2 to 4 is less than 2%, which is negligible. However, as the rise in nozzle-to-plate separation is beyond H/D>4, the decrease in the pressure was significant and maximum. Also, it has been observed that for a given Re, an increase in the H/D resulted in a decline of Cp, with a maximum of Cp occurring at H/D=1 and a minimum at H/D=6.

A similar trend is observed for all P/D. It concludes that relatively more pumping power is needed at H/D=1 to 4 and less pumping power at H/D>4, irrespective of Re and P/D. An increase in the distance between the nozzles resulted in a decrease in the drop in the Cp, with average values of 19.21%, 18.16%, and 20.76% at P/D=2, 3, and 4, respectively, from H/D=4 to 6.

**Nusselt Number (Nu)**

The influence of Re, H/D, and P/D on the Nu along the section X-X taken along the stagnation point is presented in this section. The distribution of local Nu for the in-line jets is illustrated in Figure 6 for three separation distances (H/D=1, 4, and 6), three nozzle-to-nozzle spacings (P/D=2, 3, and 4), and all Reynold's number (Re=3512.69 to 9532.71). At the stagnation point, the Nu is observed to be maximum, called the primary peak for all H/D, P/D, and Re. At H/D=1, the intensity of turbulence is higher due to the intense mixing of jets above the target plate and on the plate in the wall jet region. This created a transition in flow from the laminar to turbulence, due to which the fluctuations in the Nu are higher, as visible in Figures 6(a) and 6(b). This phenomenon is observed from Re=3512.69 to 9532.71. At this H/D=1 and P/D=2& 3, a specific peak in Nu is not observed at the point of stagnation of each jet on the impingement surface; instead, it is observed at a distance 0.6-0.8 times the nozzle diameter from the stagnation

point. With an enhancement of Reynold's number, the value of the primary peak in Nu is observed to be increasing, having a maximum at Re=9532.71. Also, a secondary peak in Nu due to interaction between the jets in the wall jet region is not visible up to Re<9532.71, and beyond this, it is visible from P/D>3. As the P/D increased, the interference of adjacent jets away from the plates before striking and interaction between the jets in the wall jet zone decreased considerably, thereby reducing the intensity of turbulence on the target plate. Still, the peak Nu varies less than 5%, increasing the P/D from 2 to 4.

As the spacing between the target plate and nozzle (H/D) increased, the entrainment losses increased, leading to a decrease in the decay of jet velocity striking the plate. However, the jet distributes over a large surface area, resulting in more cooling of the plate and lower surface temperature. This reduces the turbulence intensity on the plate, and the fluctuations in the Nu distribution on the plate are less, as compared to H/D=1.The laminar boundary layer is seen up to X/D=1.25 at the increased nozzle-to-plate separation distance, and instabilities in the Nu distribution are seen between 2.5>X/D>1.25, which may be caused by the boundary layer flow switching from laminar to turbulent. For the X/D>2.5, due to the turbulent boundary layer, a smooth variation in the Nu is noticed. However, the transition phenomenon is not recognizable at higher nozzle-to-plate distances, H/D>4, as reported by Attalla et al. [13]. Also, as the Re increases, the effect of turbulence is minimal at the central jet, and hence, a specific peak is observed at P/D=4 for H/D=4. At H/D=6, the impact of turbulence was further diminished; as a result, a primary peak in Nu is seen for all Re and P/D, whereas a particular second peak in Nu is seen for all Re at P/D=4. Also, at H/D>4 and P/D=4, more entrainment towards the central jet from the wall jet region is observed from the velocity distribution in Figures 3(f) to 3(j). This reduced the thickness of the shear layer surrounding the potential core region, thus promoting turbulence at the stagnation point. This increased the primary peak at the stagnation point corresponding to the middle jet, higher than that of the outer jets. A similar phenomenon is observed at H/D=6 in Figures 6(f) and 6(h). The maximum of Nu and $Nu_{avg}$ are observed at H/D=6 for all Re, P/D=4. This agrees with Attalla et al. [13].

It is visible from Figures 7(b) and 7(c), at P/D=3 and P/D=4, the $Nu_{avg}$ initially diminished from H/D=1 to 2 for all Re and then increased from H/D=2 to 6 at P/D=3. In contrast, at P/D=4, the $Nu_{avg}$ increased from H/D=2 to 4 and remained constant from H/D>4. As the distance between the jets increases, the $Nu_{avg}$ increases with Re from 3512.69 to 9532.71 and at H/D=1 to 6. As the Re increases from 3512.69 to 9532.71, the increase in $Nu_{avg}$ for P/D=2 is 99.23%, 131.9%, 96.28%, and for P/D=3 is 90.07%, 113.42%, 96.22%, and for P/D=4 is 85.38%, 93.45%, 95.81% at H/D=2, 4, and 6 respectively. This shows that with an increase in the jet-to-jet distance (P/D) from 2 to 4, there occurred a
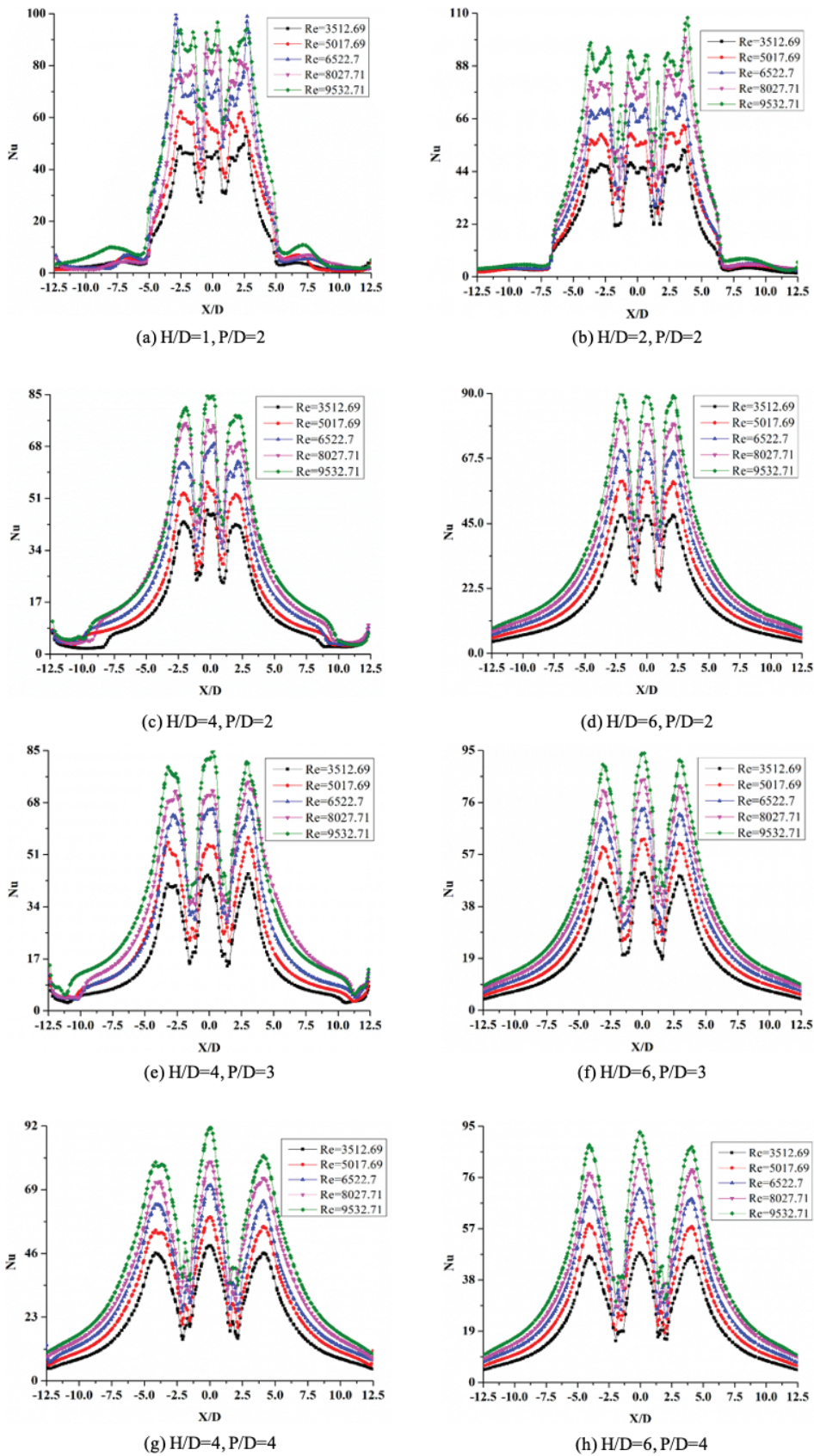
**Figure 6.** Distribution of Nu along the section x-x.

(a) P/D = 2



(b) P/D = 3



(c) P/D = 4
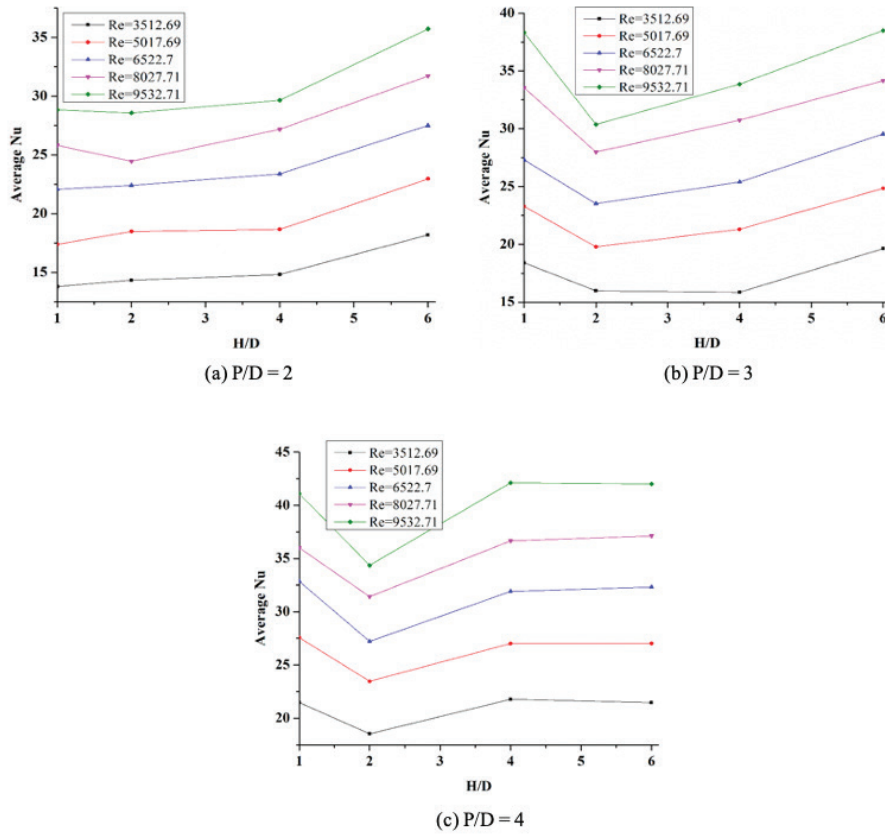
**Figure 7.** Variation of average Nusselt number.

considerable drop in the % increase in the $Nu_{avg}$ at H/D=2 &4, but for H/D=6, it is less than 1%.

ANOVA is performed to determine the significant parameter affecting the $P_{max}$, $Cp_{max}$, and $Nu_{avg}$. Regression analysis is performed with a confidence level of 98%, and correlations are developed for $P_{max}$, $Cp_{max}$, and $Nu_{avg}$ as a function of H/D, P/D, and Re, with 10-fold cross verification, and presented in eq. (14) – (16) with $R^2$ values of 99.21%, 99.60%, and 99.53%. respectively. In this analysis, the effect of interaction terms is also considered. A maximum of 12% deviation is observed between the simulation and prediction values for $Nu_{avg}$. The outcomes of the analysis of variance (ANOVA) for the $Nu_{avg}$ and $P_{max}$ are shown in Tables 4 and 5. The P/D, Re, and combination term (P/D*Re) have a significant impact on the $Nu_{avg}$. In addition, every term in the regression equation significantly impacts $P_{max}$.

$$P_{max} = -15.97\left(\tfrac{H}{D}\right) - 27.05\left(\tfrac{S}{D}\right) + 0.01779(\text{Re}) + 5.95\left(\tfrac{H}{D}\right)\left(\tfrac{S}{D}\right)$$
$$+ 0.001439\left(\tfrac{H}{D}\right)(\text{Re}) + 0.003794\left(\tfrac{S}{D}\right)(\text{Re}) \qquad (14)$$
$$- 0.000802\left(\tfrac{H}{D}\right)\left(\tfrac{S}{D}\right)(\text{Re})$$

$$C_{Pmax} = 0.2074\left(\tfrac{H}{D}\right) + 0.3463\left(\tfrac{S}{D}\right) + 0.000153(\text{Re})$$
$$- 0.07847\left(\tfrac{H}{D}\right)\left(\tfrac{S}{D}\right) - 0.000035\left(\tfrac{H}{D}\right)(\text{Re}) \qquad (15)$$
$$- 0.000047\left(\tfrac{S}{D}\right)(\text{Re}) + 0.000011\left(\tfrac{H}{D}\right)\left(\tfrac{S}{D}\right)(\text{Re})$$

$$Nu_{avg} = 1.074\left(\tfrac{H}{D}\right) + 2.503\left(\tfrac{S}{D}\right) + 0.001641(\text{Re})$$
$$- 0.305\left(\tfrac{H}{D}\right)\left(\tfrac{S}{D}\right) + 0.000078\left(\tfrac{H}{D}\right)(\text{Re}) \qquad (16)$$
$$+ 0.000331\left(\tfrac{S}{D}\right)(\text{Re})$$

**Table 4.** Model summary - ANOVA

| Parameter | S | R-sq | R-sq(adj) | R-sq(pred) | 10-fold S | 10-fold R-sq |
|---|---|---|---|---|---|---|
| $P_{max}$ | 10.4738 | 99.21% | 99.10% | 98.95% | 11.4675 | 98.93% |
| $Cp_{max}$ | 0.0659065 | 99.60% | 99.55% | 99.45% | 0.0697054 | 99.49% |
| $Nu_{avg}$ | 2.00152 | 99.53% | 99.48% | 99.43% | 2.21148 | 99.37% |

**Table 5.** Results of ANOVA

| Source | DF | | Adj SS | | Adj MS | | p | |
|---|---|---|---|---|---|---|---|---|
| | $Nu_{avg}$ | $P_{max}$ | $Nu_{avg}$ | $P_{max}$ | $Nu_{avg}$ | $P_{max}$ | $Nu_{avg}$ | $P_{max}$ |
| Regression | 6 | 7 | 46237.5 | 728395 | 7706.25 | 104056 | 0 | 0 |
| H/D | 1 | 1 | 15.5 | 1447 | 15.53 | 1447 | 0.054 | 0.001 |
| P/D | 1 | 1 | 103.1 | 10571 | 103.14 | 10571 | 0 | 0 |
| Re | 1 | 1 | 164.9 | 15944 | 164.86 | 15944 | 0 | 0 |
| H/D*P/D | 1 | 1 | 16.6 | 1624 | 16.62 | 1624 | 0.047 | 0 |
| H/D*Re | 1 | 1 | 7 | 433 | 6.98 | 433 | 0.192 | 0.052 |
| P/D*Re | 1 | 1 | 47 | 4257 | 47.03 | 4257 | 0.001 | 0 |
| H/D*P/D*Re | | 1 | | 1143 | | 1143 | | 0.002 |
| Error | 54 | 53 | 216.3 | 5814 | 4.01 | 110 | | |
| Total | 60 | 60 | 46453.8 | 734209 | | | | |

DF: Degrees of freedom; SS: Sum of the squares; MS: Mean of the squares; Adj: Adjusted.

**Comparison of Single and Multiple Jets**

Despite interference between the adjacent jets before striking the plate and interaction between the jets after hitting the plate, the characteristics of heat transfer in multiple jets are different from a single impinging jet. Figure 8(a) shows the comparison of the distribution of Nu over the target surface of a single circular jet and three inline jets for P/D = 2 to 4, at H/D=6 and Re=9532.71. For the single jet, the Nu at the stagnation point is maximum and reduces drastically along the radial direction. Also, it can be noted that the local maximum of Nu of the multiple jets, irrespective of nozzle-to-nozzle distance (P/D), is equal to that of the single jet. This trend is reported by Aldabbagh and Sezai [2] for the impingement of multiple square jets. Due to the numerous jets impinging onto the surface, more airflow over the large area of the target surface. Due to the interaction between the jets on the plate, the intensity of turbulence increases, leading to lower average air temperature. This increases the heated surface's cooling rate, with a higher heat transfer coefficient and, thus, a higher Nu. So, the higher the transfer of heat, the lower the plate's surface temperature as visible in Figures 9(a) to 9(d). Hence, the average heat transfer coefficient of the numerous impinging jets is greater than that of a single jet. The $Nu_{avg}$ recorded by the three jets with spacing P/D=2, P/D=3, and P/D=4 is 30.04%, 40.17%, and 52.96% higher than that by the single jet. This can be seen in Figure 8(b).

From Figure 10(b), the distribution of Nu is compared for P/D=2 to 5 at H/D=6 and Re=9532.71. It can be observed that the distribution of Nu is like that of a single jet. The primary peak of the Nu at the central jet is greater than the outer jets and is observed to be independent of the P/D value. With an increase in the P/D, the $Nu_{avg}$ increases for a given Re and is observed to be maximum at P/D=5. In contrast, at the
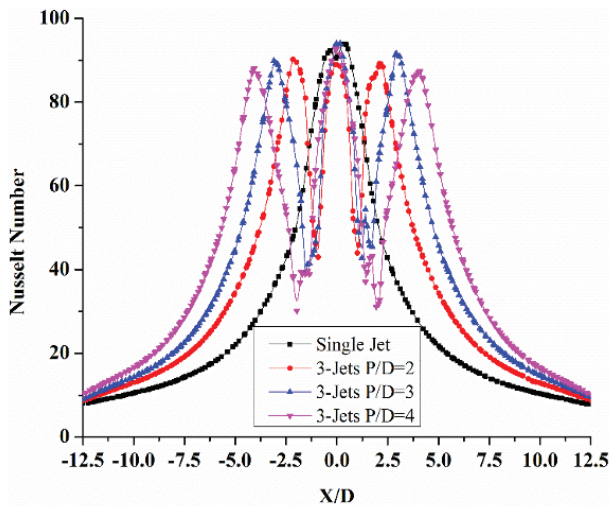


**Figure 8.** (a) Comparison of Nu distribution.
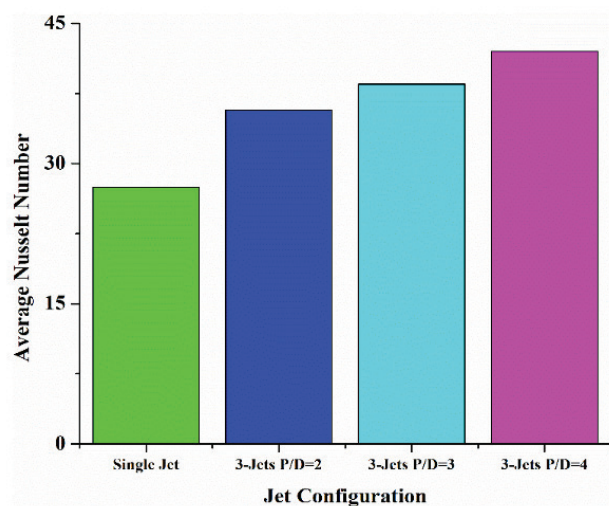


**Figure 8.** (b) Comparison of average Nusselt number.

**(a)** Single Jet             **(b)** P/D = 2

**(c)** P/D = 3             **(d)** P/D = 4
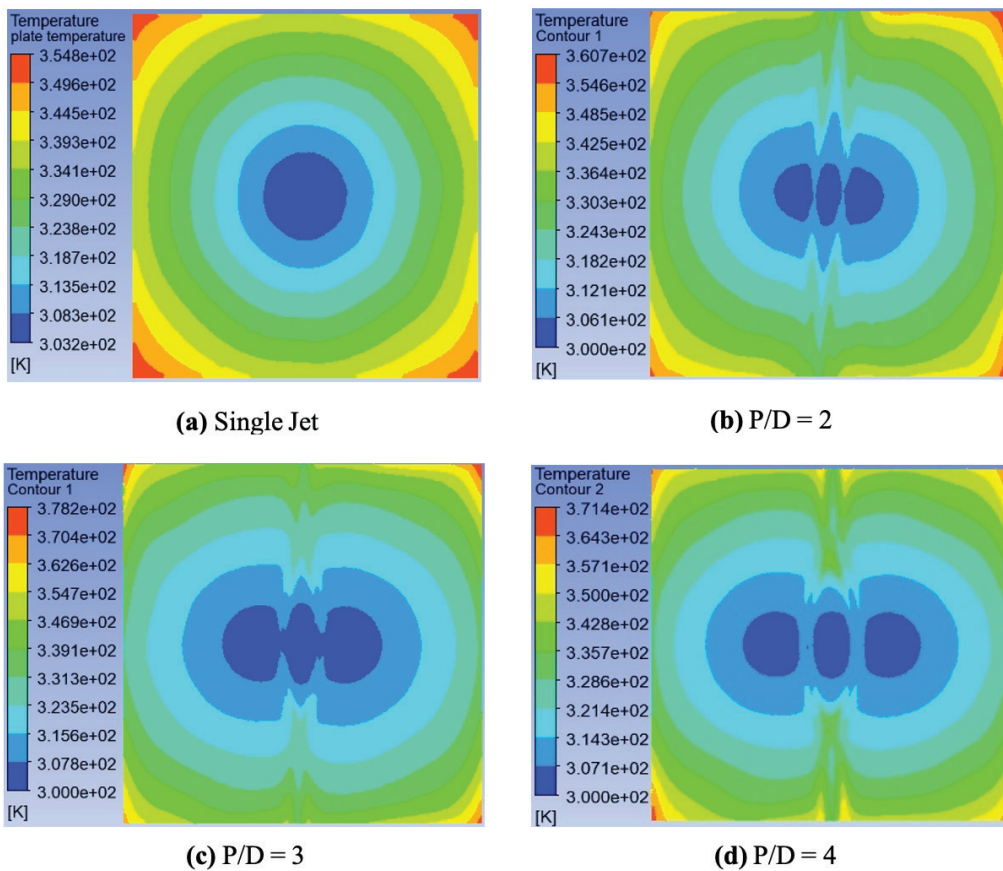
**Figure 9.** Temperature distribution.



(a)             (b)
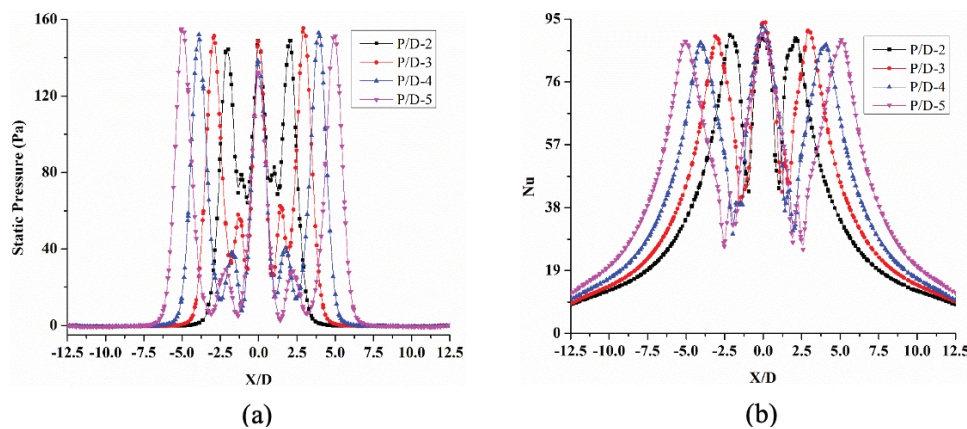
**Figure 10.** Comparison of static pressure and Nu for H/D=6, P/D=2, 3, 4, and 5 at Re=9532.71.

stagnation point corresponding to the central jet, the lowest $P_{max}$ is observed at the central jet for P/D=5. This trend is like that reported by Rama Kumar and Prasad [4].

**Flow Visualization**

This section delves into the experimental procedure followed for plotting the flow structures on the target surface

experimentally. The experiment is conducted to study the distribution of air over the target surface, during the impingement. These flow structures tell us the way heat is transferred from the hot surface to the air. Initially, using the Redwood viscometer, the kinematic viscosity of the lubricating oil (Super 20W - 40MG) is determined as 1.38 cm²/s and 1.08 cm²/s at 26⁰C and 35⁰C respectively. The

(a) P/D = 2      (b) P/D = 3      (c) P/D = 4
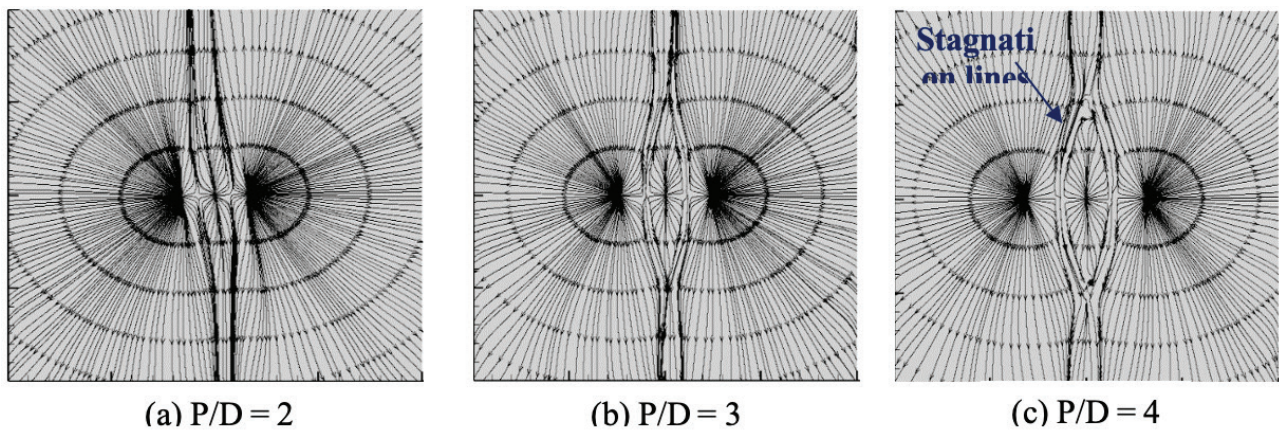
**Figure 11.** Comparison of flow structures at H/D = 6, Re = 9532.71 - Numerical analysis.

Plastic Black Carbon Powder derived from the waste plastic pyrolysis oil having a density of 1.8-2.1 gm/m$^3$ is mixed in the oil at 35$^0$C to form a slurry. The composition is chosen such that the fluidity of the slurry can capture the flow structure. It is applied as a coating of fine thickness over the target surface. Now the air is impinged on this coating. As the air flows over the coating, the carbon particles are pushed aside, and this forms the traces of air over the coated surface. After the oil is dried, images are captured using a high-definition camera having good resolution. This experiment is conducted for the Re = 3512.69, 6522.7, and 9532.71 at P/D = 4, H/D=1) and at H/D = 2, 4, and 6 for Re = 9532.71 are presented in Figures 12(b), (d), (f) and 12(h), (j) and (l) respectively.

After striking the target plate, the jet wall jets are separated from each other in the plane of impingement by a dividing stagnation line as shown in figures 11(a) to 11(c). It is visible that the outer jets are expanding towards the central jet, thus reducing the size of the central jet on the target surface. This is more prominent at lower inter-jet-spacing P/D=2. As the P/D increases, the spread of the central jet increases gradually. Also, it can be observed that there is a shift in the resultant direction of the fluid flow from the left jet to the right jet as the P/D increases from 2 to 3. This results in driving more airflow towards the right side, promoting higher heat transfer as can be seen from Figures 6(a) and 6(b). As the P/D increases, at P/D = 4, the distribution of the jet becomes symmetrical about the central jet, having the structure at the central jet as an ellipse. Because of this phenomenon, more air is entrained towards the central jet, leading to higher heat transfer at the central jet. This trend is observed at all the Re at P/D = 3 and 4, visible from the figures 6(e) to 6(h). This is similar to the temperature distribution presented in Figures 9(b)-(d). This change in the flow direction is due to the difference in the entrainment levels between the outer and inner jets at different nozzle-to-nozzle spacing.

Figures 12 (a) – 12 (e) show the comparison of flow structures obtained from the numerical analysis with those of experiments, plotted for P/D=4 and by varying H/D from 1 to 6 for different Re. At lower H/D and Re, the flow structures are observed to be complex with a greater number of eddies and recirculation flows. As the H/D increases, a curve-shaped region with a definite shape surrounding the jets is forming. At H/D>4, this shape converged into a circle around the perimeter jets, and surrounding the central jet it became an ellipse. Also, from figures 12 (b), (d), and (f), it has been observed that for the value of H/D=1 and P/D=4, with an increase in Reynold's number, the area of spread of air from the three jets increased on the target surface. This reduces the average surface temperature and increases the heat transfer rate. In addition, symmetry in the flow distribution is observed.

Also, the vortices formed around the outer jets from Figures 12 (a), (c), and (e), create low pressure around the outer jets. Hence recirculation is observed thus causing the oil to accumulate surrounding those jets from Figures 12 (b), (d), and (f). This accumulation of oil is more for Re = 9532.71, visible from Figure 12(f). As the H/D increased from 1 to 6, it can be observed that the impinging air spread over the larger area compared to the area at H/D = 1 from Figures 12 (e) to 12 (k). Hence due to more contact area, more heat could be gained by the impinging air, thus reducing the surface temperature. Hence, a higher heat transfer rate could be obtained at higher P/D, H/D, and Re.

Also, at the central jet, the shape of the structure is observed to be elliptical, as observed from the temperature distribution in Figures 9 (b) to 9 (d) and flow structures in Figures 11 (b) and 11 (c) for H/D=6, Re=9532.69, and flow structures in Figures 12 (i) to 12 (l) for H/D=4 and 6 (numerically and experimentally). Overall, the flow structures obtained numerically agree with those obtained experimentally.
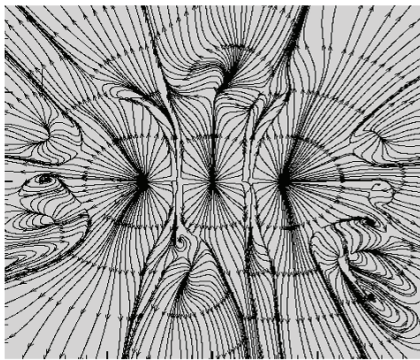
(a) H/D = 1, Re = 3521.69 Numerical
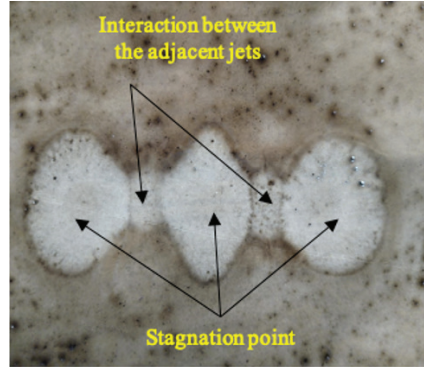


(b) H/D = 1, Re = 3521.69 Experiment
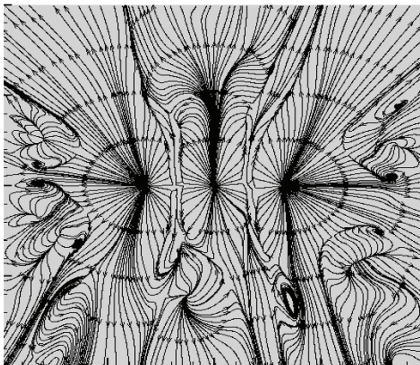


(c) H/D = 1, Re = 6522.7 Numerical
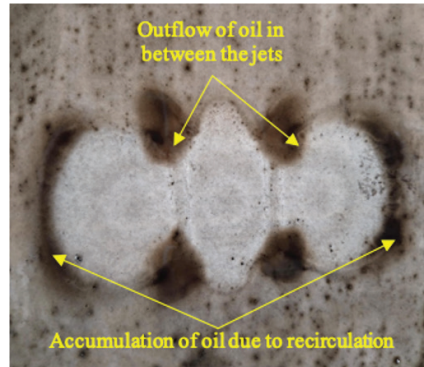


(d) H/D = 1, Re = 6522.7 Experiment
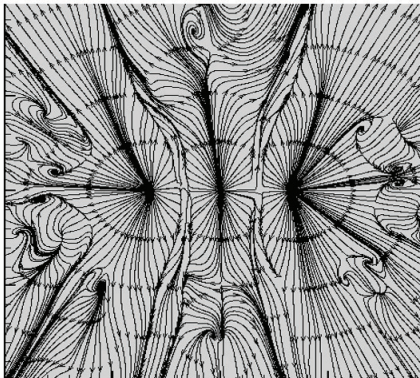


(e) H/D = 1, Re = 9532.69 Numerical



(f) H/D = 1, Re = 9532.69 Experiment
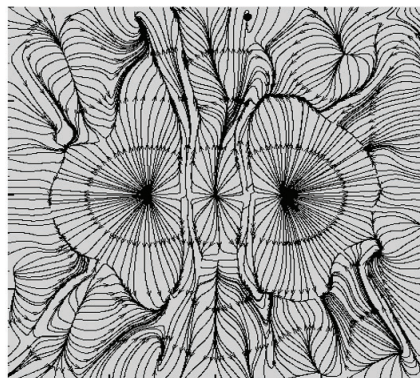


(g) H/D = 2, Re = 9532.69 Numerical



(h) H/D = 2, Re = 9532.69 Experiment

**Figure 12.** Comparison of flow structures at Re = 9532.71 obtained numerically and experimentally.

## CONCLUSION

A numerical investigation is conducted to analyze the behavior of in-line impinging circular jets for the varying dimensionless nozzle-to-plate distance from H/D=1 to 6, the nozzle-to-nozzle gap from P/D=2 to 6, and Reynold's number from Re=3512.69 to 9532.71. The flow structures obtained in the impinging of multiple jets numerically are validated by conducting the experiments. The following conclusions are drawn from this work:

1. At lower H/D, the jet is observed to fill the gap between the confinement plate and the target plate.
2. As the P/D increases from 2 to 4, and at H/D=6, two strong counter-rotating vortices surround the central jet, thus entraining the air from the outer jets towards the central jet. The effect is the thinning of the shear layer, resulting in lower $P_{max}$ and higher $Nu_{max}$ at the central jet.
3. At H/D=2 and H/D=6, minimum and maximum of $Nu_{avg}$ is observed at all P/D and Re.
4. With a confidence level of 98%, correlations are developed for $P_{max}$, $Cp_{max}$, and $Nu_{avg}$ as a function of H/D, P/D, and Re.
5. Higher the value of H/D and P/D for all Re, the higher will be the $Nu_{avg}$.
6. Less pumping power is needed at H/D>4 and higher at H/D<4. An increase in the distance between the nozzles resulted in a decrease in the drop in the Cp, with average values of 19.21%, 18.16%, and 20.76% at P/D=2, 3, and 4, respectively, from H/D=4 to 6.
7. $P_{max}$ and $Nu_{avg}$ are strongly influenced by the nozzle-to-nozzle distance, Reynold's number, and the interaction terms.
8. Flow structures obtained in the numerical analysis agree with those obtained experimentally.
9. The axis switchover is observed with an increase in the distance between the adjacent jets.
10. For better heat transfer over a heated surface, the inter-jet spacing should be maintained a minimum of 4 times the nozzle diameter, Reynold›s number should be high and the nozzle-to-plate spacing should be less, applicable for highly localized cooling applications.
11. The inline arrangement of three jets reported $Nu_{avg}$, with P/D=2, P/D=3, and P/D=4 spacing, is 30.04%, 40.17%, and 52.96% higher than the single jets.

Impingement of multiple jets with smaller diameters, in multiple rows called shower jets can be studied in cooling the electronic circuit boards and isothermal surfaces. Also, the impingement of hot air jets can be studied for localized heating applications.

## NOMENCLATURE

| | |
|---|---|
| $H$ | Distance between the nozzle and the target plate, mm |
| $D$ | Hydraulic diameter of the nozzle, mm |
| $H/D$ | Dimensionless nozzle-to-plate distance |
| $P$ | Distance between the adjacent nozzles, mm |
| $P/D$ | Dimensionless inter-jet spacing |
| $Re$ | Reynolds number |
| $Nu$ | Nusselt number |
| $Pmax$ | Pressure at the stagnation point, pa |
| $m$ | Mass flow rate of air through a single nozzle, kg/s |
| $K_{air}$ | Thermal conductivity of air, W/m-K |
| $k$ | Turbulent kinetic energy |
| $ui$ | Velocity components, i = 1, 2, 3 (or x, y, z) |
| $q$ | Heat flux, W/m$^2$ |
| $Ts$ | Surface temperature, $^O$C |
| $Ta$ | Jet temperature, $^O$C |
| $hx$ | Local heat transfer coefficient, Wm$^2$-K |
| $h_{avg}$ | Average heat transfer coefficient, Wm$^2$-K |
| $Nu$ | Local Nusselt number |
| $Nu_{avg}$ | Average Nusselt number |
| $R^2$ | Coefficient of determination |
| $V$ | Jet velocity, m/s |

Greek Symbols

| | |
|---|---|
| $\rho$ | Density of air, kg/m$^3$ |
| $\mu$ | Absolute viscosity, pa-s |
| $\omega$ | Specific dissipation rate |

## AUTHORSHIP CONTRIBUTIONS

Authors equally contributed to this work.

## DATA AVAILABILITY STATEMENT

The authors confirm that the data that supports the findings of this study are available within the article. Raw data that support the finding of this study are available from the corresponding author, upon reasonable request.

## CONFLICT OF INTEREST

The authors declared no potential conflicts of interest with respect to the research, authorship, and/or publication of this article.

## ETHICS

There are no ethical issues with the publication of this manuscript.

## REFERENCES

[1] Garimella SV, Schroeder VP. Local heat transfer distributions in confined multiple air jet impingement. J Electron Packag ASME 2001;123:165–172. [CrossRef]

[2] Aldabbagh LBY, Sezai I. Numerical simulation of three-dimensional laminar multiple impinging square jets. Int J Heat Fluid Flow 2002;23:509–518. [CrossRef]

[3]     Royne A, Dey CJ. Effect of nozzle geometry on pressure drop and heat transfer in submerged jet arrays. Int J Heat Mass Transf 2006;49:800–804. [CrossRef]

[4]     Rama Kumar BVN, Prasad BVSSS. Experimental investigation of flow and heat transfer for single and multiple rows of circular jets impinging on a concave surface. Proceedings of ASME Turbo Expo 2008: Power for Land, Sea, and Air, Berlin, Germany; June 9-13, 2008. GT2008-51044. pp. 921–929. [CrossRef]

[5]     Rama Kumar BVN, Prasad BVSSS. Computational flow and heat transfer of a row of circular jets impinging on a concave surface. Heat Mass Transf 2008;44:667–678. [CrossRef]

[6]     Rao GA, Kitron-Belinkov M, Levy Y. Numerical analysis of a multiple jet impingement system. Proceedings of ASME Turbo Expo 2009: Power for Land, Sea, and Air, Florida, USA; June 8-12, 2009. GT2009-59719. pp. 629–639. [CrossRef]

[7]     Rao GA, Kitron-Belinkov M, Levy Y. Heat transfer investigations in multiple impinging jets at low Reynolds number. Proceedings of ASME Turbo Expo 2010: Power for Land, Sea, and Air, Glasgow, UK; June 14-18, 2010. GT2010-22720. pp. 323–333. [CrossRef]

[8]     Afroz F, Sharif MAR. Numerical study of heat transfer from an isothermally heated flat surface due to turbulent twin oblique confined slot-jet impingement. Int J Therm Sci 2013;74:1–13. [CrossRef]

[9]     Hossain J, Tran LV, Kapat JS, Fernandez E, Kumar R. An experimental study of detailed flow and heat transfer analysis in a single row narrow impingement channel. Proceedings of the ASME Turbo Expo 2014: Turbine Technical Conference and Exposition, June 2014.GT2014-26498. [CrossRef]

[10]    Nabadavis A, Mishra DP. Numerical investigation of jet impingement heat transfer on a flat plate. Carbon Sci Technol 2016;8:1–12.

[11]    Meena HC, Reodikar SA, Vinze R, Prabhu SV. Influence of the shape of the orifice on the local heat transfer distribution between smooth flat surface and impinging incompressible air jet. Exp Therm Fluid Sci 2016;70:292–306. [CrossRef]

[12]    Shariatmadar H, Mousavian S, Sadoughi M, Ashjaee M. Experimental and numerical study on heat transfer characteristics of various geometrical arrangement of impinging jet arrays. Int J Therm Sci 2016;102:26–38. [CrossRef]

[13]    Attalla M, Maghrabie HM, Qayyum A, Al-Hasnawi AG, Specht E. Influence of the nozzle shape on heat transfer uniformity for in-line array of impinging air jets. Appl Therm Eng 2017;120:160–169. [CrossRef]

[14]    Simionescu SM, Tanase NO, Broboana D, Balan C. Impinging air jets on flat surfaces at low Reynolds number. Energy Proc 2017;112:194–203. [CrossRef]

[15]    Kannan BT, Panchapakesan NR. Effect of momentum flux distribution on multiple round jets. Aircr Eng Aerosp Technol 2018;90:452–460. [CrossRef]

[16]    Culun P, Celik N, Pihtili K. Effects of design parameters on a multi jet impinging heat transfer. Alex Eng J 2018;57:4255–4266. [CrossRef]

[17]    Barbosa FV, Sousa SDT, Teixeira SFCF, Teixeira JC. Application of Taguchi method for the analysis of a multiple air jet impingement system with and without target plate motion. Int J Heat Mass Transf 2021;176:121504. [CrossRef]

[18]    Shah S. Numerical analysis of heat transfer between multiple jets and flat moving surface. Int J Heat Mass Transf 2021;171:121088. [CrossRef]

[19]    Lahane S, Deshmukh P, Nargade M. Experimental investigation for heat transfer augmentation method of jet impingement using a fluid of different concentrations of water and ethylene glycol. J Therm Eng 2023;9:116–126. [CrossRef]

[20]    Ingole S. Temperature analysis for the horizontal target cooling with non-confined and inclined air jet. J Therm Eng 2023;9:342–355. [CrossRef]

[21]    Kilic M, Ali HM. Numerical investigation of combined effect of nanofluids and multiple impinging jets on heat transfer. Therm Sci 2019;23:3165–3173. [CrossRef]

[22]    Kilic M, Abdulvahitoglu A. Numerical investigation of heat transfer at a rectangular channel with combined effect of nanofluids and swirling jets in a vehicle radiator. Therm Sci 2019;23:3627–3637. [CrossRef]

[23]    Kilic M, Baskaya Ş. Improvement of heat transfer from high heat flux surfaces by using vortex promoters with different geometries and impinging jets. J Fac Eng Archit Gazi Univ 2017;32:693–707.

[24]    Kilic M, Ozcan O. A numerical investigation of combined effect of nanofluids and impinging jets for different parameters. J Fac Eng Archit Gazi Univ 2019;34:1501–1515.

[25]    Kukutla PR, Prasad BVSSS. Flow analysis of combined impingement and film cooled gas turbine nozzle guide vane. Proceedings of 2016 IEEE International Aerospace Conference, Yellow Stone Conference Centre, Big Sky, Montana, USA. [CrossRef]

[26]    Kukutla PR, Prasad BVSSS. Network analysis of a coolant flow performance for the combined impingement and film cooled first stage of high pressure gas turbine nozzle guide vane. Proc IMechE Part G J Aerosp Eng 2023:1–13.

[27]    Kukutla PR, Prasad BVSSS. Numerical study on the secondary air performance of the film holes for the combined impingement and film cooled first stage of high pressure gas. Int J Turbo Jet Engines 2017;37:221–240. [CrossRef]

[28]    Raghu Vamsi BV, Raveendiran P, Sastry MR. Heat transfer prediction in impinging jets using artificial neural networks. JP J Heat Mass Transf 2023;36:103–142. [CrossRef]

[29]    Wilcox DC. Re-assessment of the scale-determining equation for advanced turbulence models. AIAA J 1988;26:1299–1310. [CrossRef]

[30]   Menter F, Esch T. Elements of industrial heat trans-fer predictions. Proc 16th Braz Cong Mech Eng 2001;20:117–127.

[31]   Menter FR, Kuntz M, Langtry R. Ten years of industrial experience with the SST turbulence model. In: Hanjalic K, Nagano Y, Tummers M, eds. Turbulence-Heat and Mass Transfer 4. Redding, CT: Begell House Inc.; 2003. pp. 625–632.